

The ANU WiFeS SuperNova Program (AWSNAP)

Michael J. Childress^{1,2,3*}, Brad E. Tucker^{1,2}, Fang Yuan^{1,2}, Richard Scalzo¹, Ashley Ruiter^{1,2}, Ivo Seitzzahl^{1,2}, Bonnie Zhang¹, Brian Schmidt¹, Borja Anguiano⁴, Suryashree Aniyani¹, Daniel D. R. Bayliss^{1,5}, Joao Bento¹, Michael Bessell¹, Fuyan Bian¹, Rebecca Davies¹, Michael Dopita¹, Lisa Fogarty⁶, Amelia Fraser-McKelvie^{7,8}, Ken Freeman¹, Rajika Kuruwita¹, Anne M. Medling¹, Simon J. Murphy¹, Simon J. Murphy^{6,9}, Matthew Owers^{4,10}, Fiona Panther^{1,2}, Sarah M. Sweet¹, Adam D. Thomas¹, George Zhou^{11,1}

¹Research School of Astronomy and Astrophysics, Australian National University, Canberra, ACT 2611, Australia

²ARC Centre of Excellence for All-sky Astrophysics (CAASTRO)

³School of Physics and Astronomy, University of Southampton, Southampton, SO17 1BJ, UK

⁴Department of Physics and Astronomy, Macquarie University, NSW 2109, Australia

⁵Observatoire Astronomique de l'Université de Genève, 51 ch. des Maillettes, 1290 Versoix, Switzerland

⁶Sydney Institute for Astronomy (SIfA), School of Physics, The University of Sydney, NSW 2006, Australia

⁷School of Physics and Astronomy, Monash University, Clayton, Victoria 3800, Australia

⁸Monash Centre for Astrophysics (MoCA), Monash University, Clayton, Victoria 3800, Australia

⁹Stellar Astrophysics Centre, Department of Physics and Astronomy, Aarhus University, 8000 Aarhus C, Denmark

¹⁰Australian Astronomical Observatory, PO Box 915, North Ryde, NSW 1670, Australia

¹¹Harvard-Smithsonian Center for Astrophysics, 60 Garden St, Cambridge, MA 02138, USA

Abstract

This paper presents the first major data release and survey description for the ANU WiFeS SuperNova Program (AWSNAP). AWSNAP is an ongoing supernova spectroscopy campaign utilising the Wide Field Spectrograph (WiFeS) on the Australian National University (ANU) 2.3m telescope. The first and primary data release of this program (AWSNAP-DR1) releases 357 spectra of 175 unique objects collected over 82 equivalent full nights of observing from July 2012 to August 2015. These spectra have been made publicly available via the WISEREP supernova spectroscopy repository.

We analyse the AWSNAP sample of Type Ia supernova spectra, including measurements of narrow sodium absorption features afforded by the high spectral resolution of the WiFeS instrument. In some cases we were able to use the integral-field nature of the WiFeS instrument to measure the rotation velocity of the SN host galaxy near the SN location in order to obtain precision sodium absorption velocities. We also present an extensive time series of SN 2012dn, including a near-nebular spectrum which both confirms its “super-Chandrasekhar” status and enables measurement of the sub-solar host metallicity at the SN site.

Keywords: supernovae: general; supernovae: individual (SN 2012dn)

1 Introduction

In the last decade, wide-field extragalactic transient surveys – such as the Palomar Transient Factory (PTF; Rau et al. 2009; Law et al. 2009), the Panoramic Survey Telescope and Rapid Response System (PanSTARRS; Kaiser et al. 2010), the Catalina Real-time Transient Survey (CRTS; Drake et al. 2009), and the Texas Supernova Search (Quimby 2006; Yuan 2010) – have revolutionised our understanding of the myriad ways in which stars explode through the discovery of new classes of exotic transients. Simultaneously, these surveys have discovered hundreds of supernovae (SNe) of “traditional” types (see Filippenko 1997, for a review), enabling statistical analyses of the properties of these SNe.

While imaging surveys have provided discovery and light curves for this wealth of new transients, complementary spectroscopy surveys have provided the critical insight into the physical origins of these events. Numerous supernova spectroscopy surveys have released thousands of high quality spectra of nearby SNe into the public domain (Matheson et al. 2008; Blondin et al. 2012; Silverman et al. 2012c; Folatelli et al. 2013; Modjaz et al. 2014). These surveys have frequently been dedicated to the spectroscopic followup of Type Ia supernovae (SNe Ia) which, due to their rates and luminosities, dominate any magnitude-limited imaging survey. Such surveys have revealed that photometrically similar SNe can still exhibit diversity of spectroscopic behaviour, indicating spectra remain a critical tool for revealing the full nature of the supernova progenitors

*E-mail: m.j.childress@soton.ac.uk

(particularly for SNe Ia). Additionally, spectra remain critical for supernova classification – particularly at early phases when the full photometric evolution has yet to be revealed. Such early classifications then inform the use of additional SN followup facilities, including those operating outside the optical window.

Recently the Public ESO Spectroscopic Survey for Transient Objects (PESSTO; Smartt et al. 2015) began a multi-year program on the NTT 3.6m telescope in Chile, with the goal of obtaining high quality spectral time series for roughly 100 transients (of all kinds) to be released to the public. This survey has already released hundreds of spectra in its first two annual data releases, and continues to release all SN classification spectra within typically 1 day from observation. Other ongoing SN spectroscopy programs, such as the Asiago Supernova Program (Tomasella et al. 2014), also make important contributions to the transient community through timely SN classification and spectroscopy releases.

Here we describe our ongoing spectroscopy program AWSNAP – the **ANU WiFeS SuperNovA Program** – which uses the Wide Field Spectrograph (WiFeS; Dopita et al. 2007, 2010) on the Australian National University (ANU) 2.3m telescope at Siding Spring Observatory in Australia. In this paper we describe the data processing procedures for this ongoing program, and describe the first AWSNAP data release (AWSNAP DR1) comprising 357 spectra of 175 supernova of various types obtained during 82 classically-scheduled observing nights over a 3 year period from July 2012 to August 2015. Most of these spectra have been released publicly via the Weizmann Interactive Supernova data REpository (WiSeREP¹ – Yaron & Gal-Yam 2012), with the remainder set to be released within the next year as part of forthcoming PESSTO papers. This program will continue to observe SNe of interest and classify SN discoveries from transient searches such as the new SkyMapper Transients Survey (Keller et al. 2007). We aim to release future SN classification spectra from AWSNAP publicly via WiSeREP in parallel with any classification announcements.

This paper is organised as follows. Section 2 describes the WiFeS data processing and SN spectrum extraction procedures. Section 3 presents general properties of our SN sample and compares AWSNAP DR1 to other public SN spectra releases. In Section 4 we present some analysis of the properties of the SNe Ia in our sample, including measurement of narrow sodium absorption features afforded by the intermediate resolution of the WiFeS spectrograph. Some concluding remarks follow in Section 5.

2 Observations and Data Description

Observations for AWSNAP were conducted with the Wide Field Spectrograph (WiFeS – Dopita et al. 2007, 2010) on the Australian National University 2.3m telescope at Siding Spring Observatory in northern New South Wales, Australia. Observing nights were classically scheduled with a single night of observing every 8-15 days. On some occasions, special objects of interest were observed during non-AWSNAP nights. A full list of the AWSNAP transient spectra is presented in Table 6 in Appendix A. In the sections that follow, we describe the processing of the WiFeS data, then characterise both the long term performance of the WiFeS instrument and observing conditions at Siding Spring.

2.1 Data Reduction and Supernova Spectrum Extraction

The WiFeS instrument is an image-slicing integral field spectrograph with a wide $25'' \times 38''$ field of view. For AWSNAP, this frequently provided simultaneous integral field observations of SNe and their host galaxies. The WiFeS image slicer breaks the field of view into 25 “slitlets” of width $1''$, which then pass through a dichroic beamsplitter and volume phase holographic (VPH) gratings before arriving at $4k \times 4k$ CCD detectors. AWSNAP observations were always conducted with a CCD binning of 2 in the vertical direction – this sets the vertical spatial scale of the detector to be $1''$, yielding final integral field elements (or “spaxels”) of size $1'' \times 1''$. Typically seeing at Siding Spring is roughly $2''$ (see Section 2.3).

The VPH gratings utilised by WiFeS provide a higher wavelength resolution than traditional glass gratings. The low- and high-resolution gratings provide resolutions of $R = 3000$ and $R = 7000$, respectively, yielding velocity resolutions of up to $\sigma_v \sim 45 \text{ km s}^{-1}$ which is ideal for observing nebular emission lines from ionised regions in galaxies. For supernovae, this can reveal narrow absorption features (see Section 4.2) from circumstellar material (CSM) which are typically smeared out by lower resolution spectrographs. AWSNAP observations were generally conducted with the lower resolution B3000 and R3000 gratings for the blue and red arms of the spectrograph, respectively, with the RT560 dichroic beamsplitter. Occasionally the R7000 grating was deployed on the red arm to provide higher resolution observations of sodium absorption features. In Table 1 we provide the wavelength range, spectroscopic pixel size, and wavelength resolution (determined as the FWHM of calibration lamp emission lines) for the three gratings used for AWSNAP observations.

Data for AWSNAP observations were reduced with version 0.7.0 of the PyWiFeS pipeline (Childress et al. 2014b). PyWiFeS performs standard image pre-

¹<http://wiserep.weizmann.ac.il>

Table 1 Details of WiFeS gratings.

Grating	λ_{min}	λ_{max}	Pixel size	Resolution
B3000	3500 Å	5700 Å	0.77 Å	1.5 Å
R3000	5400 Å	9570 Å	1.25 Å	2.5 Å
R7000	5400 Å	7020 Å	0.44 Å	0.9 Å

processing such as overscan and bias subtraction, as well as cosmic ray rejection using a version of LACosmic (van Dokkum 2001) tailored for WiFeS data. The wavelength solution for WiFeS is derived using an optical model of the spectrograph which achieves an accuracy of 0.05 to 0.10 Å (for $R = 7000$ and $R = 3000$, respectively) across the entire detector. Spectral flatfielding (i.e. correction of pixel-to-pixel quantum efficiency variations) is achieved with an internal quartz lamp, while spatial flatfielding across the full instrument field of view is facilitated by twilight sky flats. Once the data has been preprocessed and flat-fielded, it is resampled onto a rectilinear three-dimensional (x, y, λ) grid (a “data cube”). We then flux calibrate the data cubes with the use of spectrophotometric standard stars (from, e.g., Oke 1990; Bessell 1999; Stritzinger et al. 2005) and the Siding Spring Observatory extinction curve from Bessell (1999), while telluric features are removed using observations of smooth spectrum stars.

To further facilitate data reduction for the AWSNAP data release, we developed an SQL database for WiFeS observations using the Python Django framework. We created modified versions of the PyWiFeS reduction scripts that allow the user to request that all data from a specific night using a specific grating be fully reduced. The reduction scripts then query the database for all science observations and calibration data from that night and perform the required reduction procedures. For nights where a full suite of calibrations was not available (e.g. due to guest observations on a non-AWSNAP night), calibration solutions from the closest (in time) AWSNAP night were automatically identified via the database and employed in the reduction. Both the wavelength solution and spatial flatfielding of the instrument are incredibly stable on long (\sim year) timescales (see Section 2.2), thus validating the choice to use calibrations from different nights where necessary. This new database-driven data processing mode for PyWiFeS will be an important component of the upcoming effort to develop fully robotic queue-based observing capabilities for the ANU 2.3m telescope.

The output of the PyWiFeS pipeline is a flux calibrated data cube that contains signal from the target supernova, the night sky, and occasionally the SN host galaxy. Extraction of the SN spectrum requires isolation of the spaxels containing supernova signal and subtraction of the underlying sky (and possibly galaxy) background. To achieve this, we constructed a cus-

tom Python-based GUI which allows the user to manually select spaxels containing the target SN (“object” spaxels) and spaxels used to determine the background (“sky” spaxels, which may contain some galaxy signal). The background spectrum is determined as the median spectrum across all “sky” spaxels, and this median spectrum is subtracted from each “object” spaxel. The final SN spectrum is then the sum of the sky-subtracted object spaxels, and the variance spectrum is the sum of the variance from all object spaxels (with no subtraction of sky variance).

This SN spectrum extraction technique produces excellent quality sky subtraction due to the robust spatial flatfielding achieved with PyWiFeS. However, some obvious sky subtraction residual features are evident in the redder wavelengths of most R3000 spectra where the night sky exhibits sharp emission features from rotational transitions of atmospheric OH molecules. The intrinsic line width of these emission lines is below the resolution of the spectrograph, meaning the observed line width is that of the spectrograph – which in this case is only slightly larger than the detector pixel size. The natural wavelength solution of the spectrograph shifts spaxel-to-spaxel, so when all spaxels are resampled onto the same wavelength grid this means sky lines experience pixel-wise resampling that is not uniform across the full instrument field of view. Thus when a median sky spectrum is subtracted from a specific spaxel, some residual features arise due to this resampling effect. A more robust technique for correcting this would be to model the intrinsic sky spectrum using the multiple samplings achieved across all spaxels and resample it to the wavelength solution of each spaxel before subtracting it (as was demonstrated for two-dimensional spectroscopic data by Kelson 2003). Such a technique is beyond the scope of the current data release, but is being prioritised for future AWSNAP releases.

2.2 Long-Term Behaviour of the WiFeS Instrument

One key advantage of having a long-running observing program is the ability to characterise the long term behaviour of the WiFeS instrument. Below we analyse the stability of the wavelength solution and instrument throughput on multi-year timescales. WiFeS did undergo a major change in early 2013 when the detectors for both arms of the spectrograph were replaced with higher throughput E2V CCDs. Thus we restrict our analysis to dates from late May 2013 until the end of the current data release in August 2015.

We collected the wavelength solution fits for the B3000 (R3000) grating from 48 (45) distinct epochs following the WiFeS detector upgrade. In Figure 1 we plot the difference between the wavelength solution for each individual epoch and the mean wavelength solu-

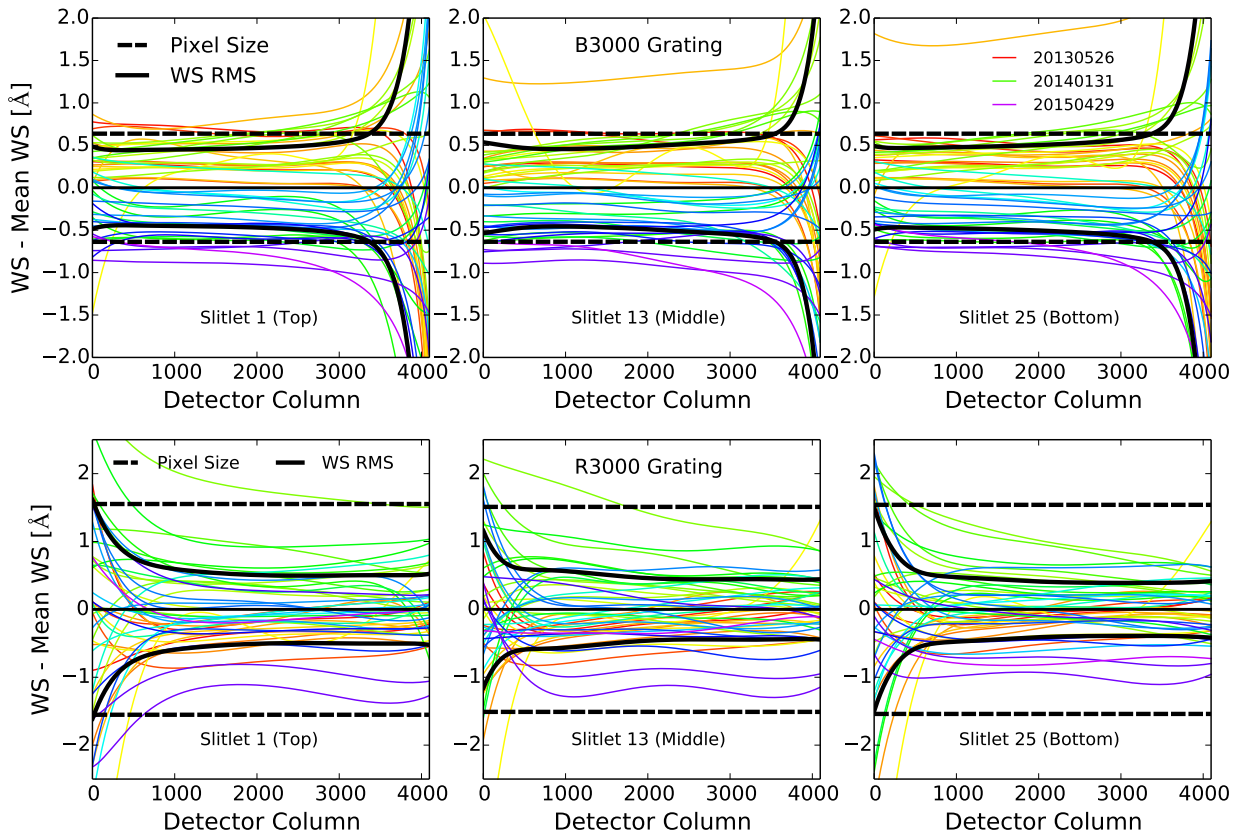


Figure 1. Evolution of the WiFeS wavelength solution over a 2-year period spanning May 2013 to April 2015. In each panel we plot the deviation of individual wavelength solutions from the mean solution (averaged over the full 2-year period) for the top, middle, and bottom slitlets of the instrument (left, middle, and right columns, respectively) for the B3000 (top row) and R3000 (bottom row) gratings. Wavelength solution residuals are colour-coded by date from earliest (red) to latest (purple), with the pixel size (dashed black lines) and wavelength solution residual RMS (solid black lines) displayed for comparison.

tion across all epochs. Epochs are colour-coded from earliest (red) to latest (purple) to illustrate potential coherent long-term shifts in the wavelength solution. The top panels present the B3000 grating, while the bottom panels present the R3000 gratings. The three columns represent the WiFeS slitlets at the top, middle, and bottom of the detectors.

From these plots we see clear demonstration of the remarkable stability of the WiFeS instrument. The RMS variation of wavelength solution is smaller than a single pixel for both gratings (i.e. both detectors) for nearly all wavelengths, with the exception of the lower throughput regions near the dichroic boundary. There is some evidence of a coherent shift of the blue detector wavelength solution over the two year time period probed here, but this is still less than two pixels shift. For the red detector, we can say confidently that *the wavelength solution has shifted by less than a pixel over a timescale of two years*. This remarkable stability achieved (by design) by WiFeS means the use of the wavelength solu-

tion from an adjacent night yields negligible changes in wavelength, and thus small instrumental velocity shifts – highly suitable for supernova analyses.

We then collected illumination corrections (derived from twilight flat observations) from 46 (45) distinct epochs for the B3000 (R3000) grating. In Figure 2 we show the mean illumination correction (left panels) and RMS of the illumination correction (rights panels – presented in fractional form, i.e. the RMS divided by the mean) for both the B3000 (top) and R3000 (bottom) gratings. We find the mean variation of the illumination correction to be 1.4% and 1.2% for the B3000 and R3000 gratings, respectively, for the full WiFeS field of view. For the innermost $8'' \times 8''$ region typically used for SN observation in AWSNAP, the RMS of the illumination correction is 0.8% and 0.3% for the blue and red detectors (i.e., B3000 and R3000 gratings). Thus the throughput of the WiFeS instrument has remarkable spatial uniformity on long (multi-year) timescales.

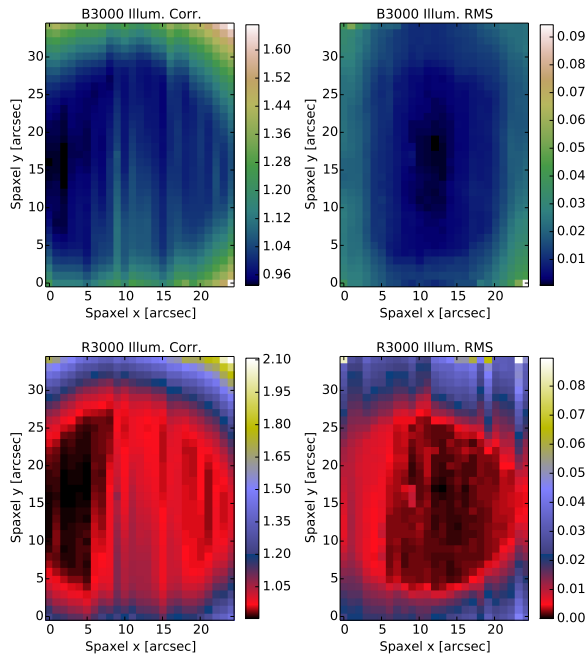


Figure 2. The normalised mean (left column) and RMS (right column) of the illumination corrections for the B3000 (top row) and R3000 (bottom row) gratings. The RMS images are shown as fractional values of the mean illumination correction.

2.3 Observing Conditions at Siding Spring Observatory

In addition to the long-term behaviour of the WiFeS instrument, our observing program allows us to monitor the observing conditions at Siding Spring Observatory. Below we briefly discuss the atmospheric throughput and seeing conditions experienced during AWSNAP observing.

We collected the flux calibration solutions from 59(54) epochs for the B3000 (R3000) grating from May 2013 to August 2015, and these are plotted in Figure 3 after being normalised in the wavelength range with highest throughput (4500-5400 Å and 6500-8000 Å for B3000 and R3000, respectively). These curves represent the normalised throughput (in magnitudes) of the instrument and atmosphere as measured with spectrophotometric standard stars (typically from Oke 1990; Bessell 1999; Stritzinger et al. 2005) whose flux has already been corrected using the nominal Siding Spring extinction curve from Bessell (1999). The effects of the instrument throughput and atmospheric transmission are degenerate here, as WiFeS instrument throughput cannot be independently measured using local (i.e. terrestrial) calibration sources.

From the curves in Figure 3, we see that the total combined throughput of the instrument plus at-

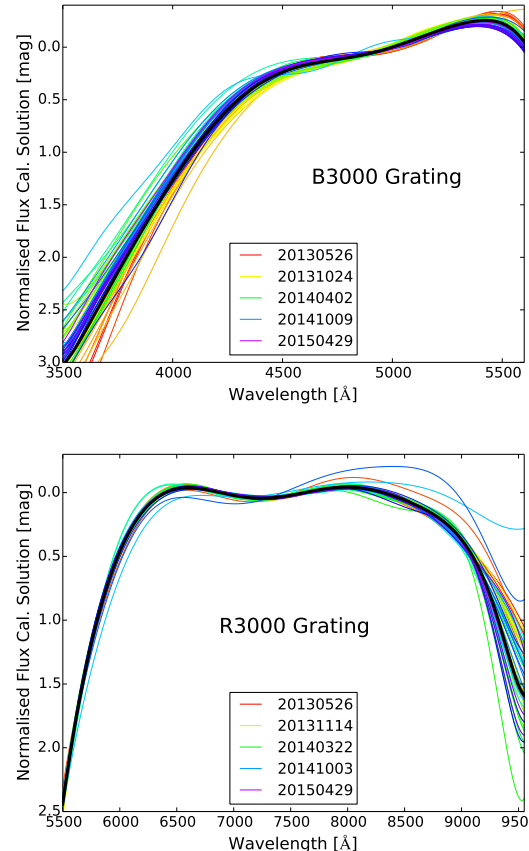


Figure 3. Flux calibration solutions for the B3000 (top) and R3000 (bottom) gratings. As in Figure 1, these are colour-coded by date from earliest (red) to latest (purple), with the mean flux calibration solution shown as the solid black line.

mosphere is relatively stable. We calculated the RMS colour variation in the throughput curves and find variations of $\sigma(U - B) = 0.09$ mag for B3000 (note the V band runs into the wavelength range where the dichroic splits light between the blue and red channels) and $\sigma(r - i) = 0.04$ mag for R3000. We note these are calculated from the mean flux calibration solution for each night, where no attempt has been made to derive a unique extinction curve for a given night. These colour variations are relatively small, and comparable in size to the colour dispersion found when comparing spectrophotometry to imaging photometry for other SN spectroscopy samples (e.g., Silverman et al. 2012c; Blondin et al. 2012; Modjaz et al. 2014).

We also measured the atmospheric seeing during our observing program, using both guide star FWHM measurements recorded from the WiFeS guider camera and low airmass ($secz \leq 1.5$) WiFeS data cubes convolved with the B - and R -band filter curves (for the blue and

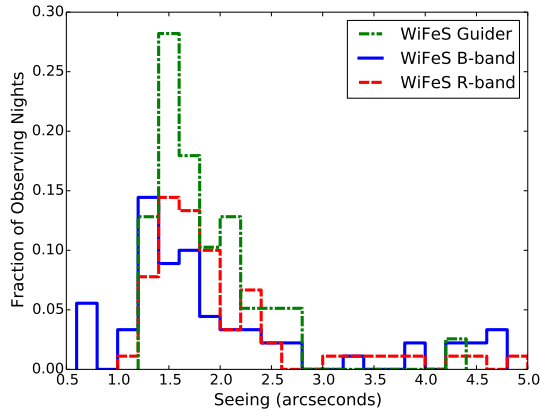


Figure 4. Seeing measurements at Siding Spring Observatory as measured during AWSNAP observations. These include measurements from the WiFeS guider camera (green dash-dot histogram), and measurements of low airmass standard star WiFeS datacubes convolved with *B*-band (blue solid histogram – from the blue detector) and *R*-band (red dashed histogram – from the red detector) filter curves.

red cameras, respectively). We plot the observed distribution of seeing values in Figure 4. The seeing distribution peaks slightly above $1.5''$ (for all measurements) with a tail predominantly filled to $2.5''$, with little or no sub-arcsecond observations and a small number of observations with incredibly poor seeing ($3.0''$ or greater).

3 The AWSNAP Supernova Sample and Spectroscopic Data Release

In this Section we briefly describe the global characteristics of the sample of SNe comprising the first data release (DR1) for AWSNAP. This consists of observations made between 18 July 2012 and 17 August 2015, a total of 357 epochs of 175 total SNe. These spectra have all been uploaded to WISEREP (Yaron & Gal-Yam 2012), with most made publicly available and the small remainder set to be made public with the associated PESSTO publication within the next year. Some additional spectra taken after 17 August 2015 have been processed and released via WISEREP, and we expect the future release of AWSNAP spectra to proceed in a continuous fashion via the same procedures outlined in this work.

The observing and target selection strategy for AWSNAP DR1 was heavily influenced by the scheduling of our observing time, which typically consisted of one single classically-scheduled full night of observing every 8-15 days throughout the entirety of the calendar year. The most significant implication of this schedul-

ing was that dense spectroscopic sampling (i.e., 2-3 day cadence) was generally not viable for our preferred targets. Furthermore, additional targets were always needed to fill an entire night of observing. Thus we frequently chose to make complementary observations of targets being observed through the PESSTO program (Smartt et al. 2015), or chose targets whose spectroscopic data would have legacy value for future analyses. As a result, we observed a diverse range of targets that covered the entire Southern sky. The full list of targets and their classification information is presented in Table 4 in Appendix A, and their distribution on the sky is shown in Figure 5.

In Figure 6 we present a histogram of the number of spectroscopic observations per target for the AWSNAP sample compared to three major SN Ia spectroscopic data releases: the Berkeley SN Ia Program (BSNIP; Silverman et al. 2012c), the Harvard Center for Astrophysics (CfA) supernova program (Matheson et al. 2008; Blondin et al. 2012), and the Carnegie Supernova Project (CSP; Folatelli et al. 2013). Our sample has a high fraction of singly-observed targets compared to the other programs. This is in part due to the fact that our data release includes all our SN classification spectra, as well as the persistent need for us to fill our classically-scheduled observing queue. We thus also show in the inset of Figure 6 the normalised histogram of spectroscopic epochs for multiply-observed SNe (i.e. targets with $N_{obs} > 2$), which shows a much more similar distribution to the other programs.

The types of SNe observed in AWSNAP DR1 is summarized in Table 2 and presented graphically in Figure 7. For this, we have grouped the SNe by type into four main categories:

- SNe Ia: includes the standard (“Branch-normal”) SNe Ia, subluminous (SN 1991bg-like Filippenko et al. 1992b), overluminous (SN 1991T- and SN 1999aa-like Filippenko et al. 1992a), candidate “super-Chandrasekhar” SNe Ia (Scalzo et al. 2010, 2012), and SNe Iax (Foley et al. 2013)
- SNe Ibc: SNe Ic, SNe Ib and SNe Iib – the standard classes of “stripped-envelope” SNe (e.g. Bianco et al. 2014; Modjaz et al. 2014; Graur et al. 2015; Liu et al. 2015)
- SNe II: SNe IIP and SNe IIL – which we note cannot be distinguished spectroscopically – and SNe IIn
- SLSNe: “superluminous” supernovae – for our sample this consists entirely of the “SLSN-Ic” type (see, e.g., Inserra et al. 2013) which show blue continua with weak absorption features and no hydrogen signatures

AWSNAP Targets vs. Planck 857 GHz

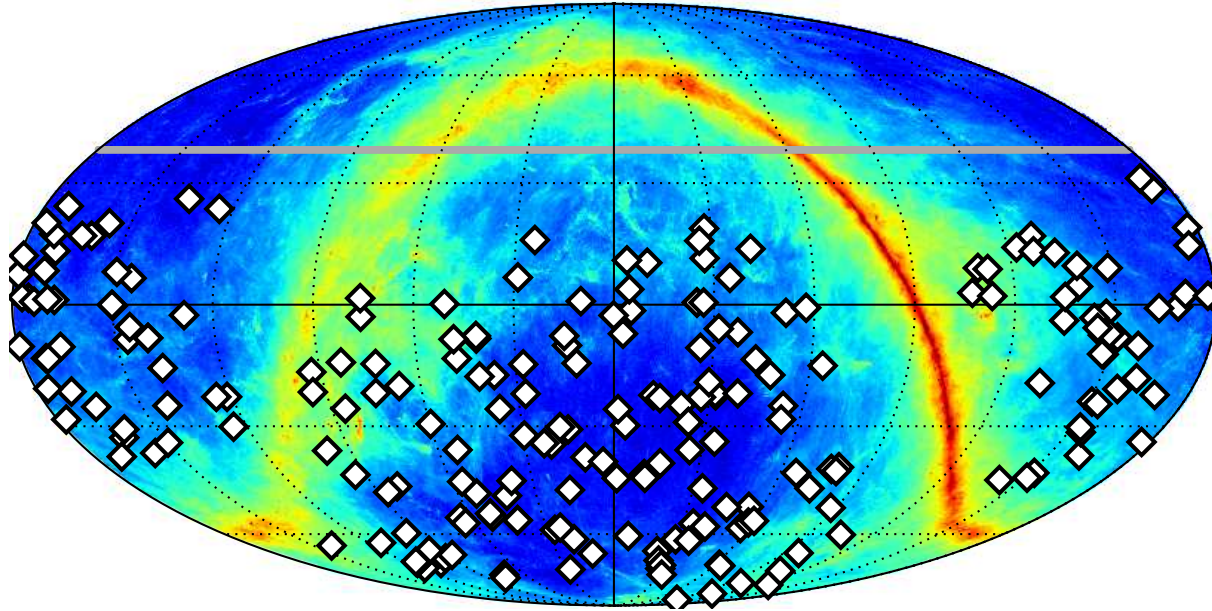


Figure 5. On-sky distribution (in equatorial coordinates) of all extragalactic targets in AWSNAP DR1 (white diamonds) plotted over the 857 GHz all-sky map from the *Planck* satellite (Planck Collaboration et al. 2011) which reveals emission by Milky Way dust. The physical pointing limit of the ANU 2.3m telescope ($\sim +40^\circ$ declination) is shown as the solid grey bar.

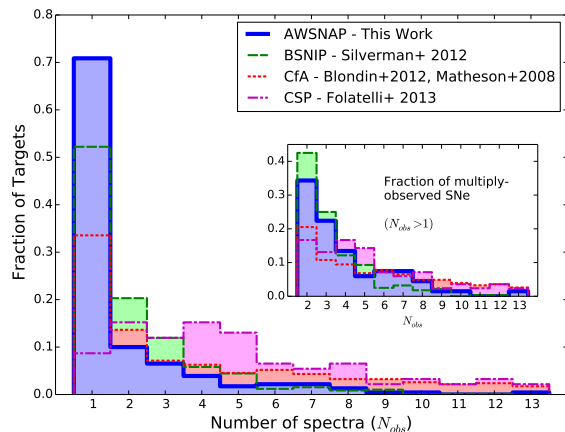


Figure 6. Normalized histogram of the number of spectroscopic epochs per target for the full sample of AWSNAP DR1 targets. For comparison we also show the same histogram for previous SN spectroscopy surveys: BSNIP (Silverman et al. 2012c), CfA (Matheson et al. 2008; Blondin et al. 2012), and CSP (Folatelli et al. 2013). The inset shows the (re-)normalized histograms of the number of spectroscopic epochs for multiply-observed targets (i.e. those with $N_{obs} > 1$) in the same surveys.

Table 2 AWSNAP objects and spectra by SN type.

SN Type	# Objects	# Spectra
SN Ia	101	180
SN II	53	117
SN Ibc	15	43
SLSN	6	17
Total	175	357

We note these groupings are made strictly to provide broad perspective on the sample statistics, but we reiterate that the SN sub-types within each group have their own unique physical mechanisms.

From Figure 7 we clearly see that, as expected, SNe Ia comprise the majority of objects and spectra in the AWSNAP sample, but comprise a smaller fraction than might be expected from a pure magnitude limited sample of SNe such as that of the Lick Observatory Supernova Search (LOSS, whose relative SN rates are presented in Li et al. 2011b). This may be due in part to the fact that many of the SNe in AWSNAP were discovered by untargeted supernova searches such as the All-Sky Automated Survey for Supernovae (ASAS-SN; Shappee et al. 2014). These surveys find SNe in low mass galaxies that are missed by targeted surveys such as LOSS. Due to the increased star-formation intensity in low mass galaxies (e.g. Salim et al. 2007) this means the relative

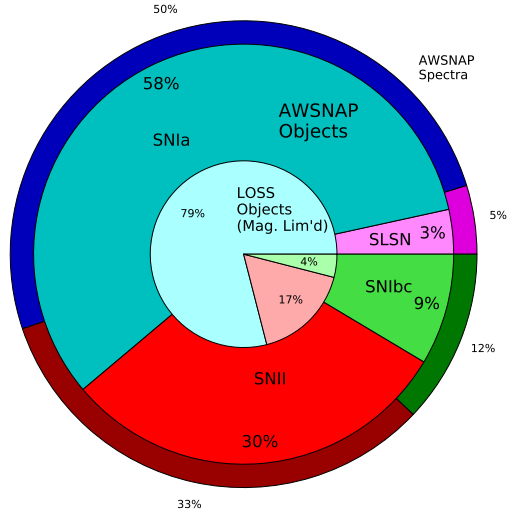


Figure 7. Total number of spectra (outer ring) and SN targets (middle annulus) for AWSNAP broken down by SN type, compared to the volume-limited SN rates (inner circle) for the LOSS survey (Li et al. 2011b, – note this galaxy-targeted survey did not find any SLSNe). In each ring the regions are colour-coded by (broad) SN type (see text for discussion): SNe Ia (blue), SNe II (red), SNe Ib/Ic (green), and SLSNe (purple).

rate of core-collapse supernovae will be higher and thus CCSNe will comprise a higher fraction of the sample. Additionally, we explicitly targeted a higher fraction of CCSN discoveries owing to the comparative paucity of CCSN spectroscopic samples compared to SNe Ia (again arising from the magnitude-limited rates).

4 Type Ia Supernova Spectra from AWSNAP

As a first demonstration of the usefulness of the AWSNAP dataset, we analyse basic spectroscopic features of the SNe Ia in our sample – this comprises 180 total spectra of 101 objects. In Figure 8 we plot a histogram of the phases² of our SN Ia spectra, again compared to previous large SN Ia spectroscopy surveys (CfA, BSNIP, CSP). Our sample shows a similar phase coverage as previous surveys, with perhaps a slight increase in earlier phases due to improved SN discovery efficiency from nearby SN searches. In the sections that follow we further analyse features of interest from the AWSNAP SN Ia spectroscopy sample.

²Based on the spectroscopically-estimated phase reported at the time of classification.

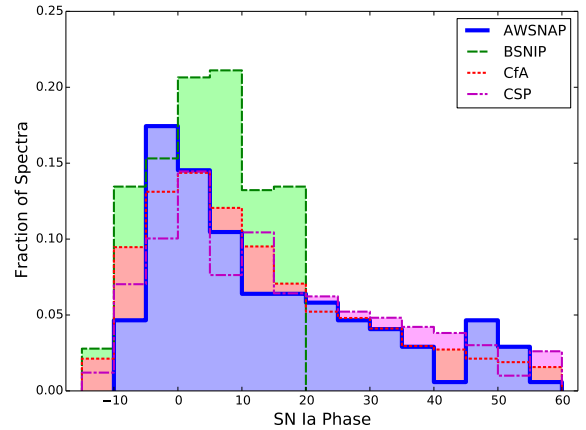


Figure 8. Histograms of spectroscopic phases (with respect to B -band maximum light) for SN Ia spectra in AWSNAP and other SN Ia spectroscopy samples (the same as in Figure 6). Note the AWSNAP phases are based on the spectroscopic-based phase reported with the SN classification, which may have an associated uncertainty of 3-5 days.

4.1 Spectral features in SNe Ia at maximum light

We begin by inspecting the spectra of SNe Ia close to the epoch of peak brightness. These maximum light spectra have a long history of providing key insights into the diversity of SN Ia explosions through the study of “spectral indicators” (Nugent et al. 1995; Hatano et al. 2000; Benetti et al. 2005; Bongard et al. 2006, 2008; Hachinger et al. 2006, 2008; Branch et al. 2006, 2009; Bronder et al. 2008; Silverman et al. 2012b), as well as potential avenues for improving the cosmological standardization of SNe Ia (Wang et al. 2009; Bailey et al. 2009; Blondin et al. 2011; Silverman et al. 2012a). Thus we actively targeted many SNe Ia (which had already been classified) on an epoch close to maximum light to obtain high quality spectra facilitating such studies.

We isolated the sample SNe Ia with a spectrum within 5 days of estimated peak brightness. It is important to reiterate here that the phases for our SN Ia sample are extrapolated from the reported spectroscopic classification phase and date. It has been demonstrated previously (e.g. Blondin et al. 2012) that the phase determined for SNe Ia via spectroscopic matching codes such as SNID (Blondin & Tonry 2007) typically has an uncertainty of at least 3-5 days. Thus we may have included SN Ia spectra as much as 10 days removed from maximum light. Our analysis here is intended to be illustrative of the utility of our published spectra, and more detailed quantitative spectroscopic analyses

should always be coupled to a robust photometric data set.

For the analysis that follows, we measure two key quantities of interest: the silicon absorption ratio R_{Si} , and the strength of high-velocity features (HVF) R_{HVF} . For this work, we define R_{Si} as the ratio of the pseudo equivalent width (pEW) of the 5962Å feature to the pEW of the 6355Å feature. The pEW for each feature is measured by fitting a linear pseudo-continuum across narrow regions redward and blueward of the given feature (similar to methods employed in Silverman et al. 2012b), then integrating the flux in the normalized absorption feature.

R_{Si} is known to correlate strongly with the SN Ia light curve decline rate (Nugent et al. 1995). We quantified the relationship between our definition of R_{Si} (the pEW ratio) and light curve decline rate Δm_{15} by fitting a linear relationship between these quantities for a sample of 342 SNe Ia collated from the CfA, BSNIP, and CSP samples. From these data we derive:

$$\Delta m_{15} = 2.04R_{Si} + 0.808 \pm 0.190 \quad (1)$$

Below we will use this relation to display the corresponding range of Δm_{15} spanned by our observed values of R_{Si} .

We measure the HVF strength for our SN Ia sample using the same techniques employed in Childress et al. (2014a), and similarly define R_{HVF} as the ratio of the pEW of the high-velocity feature (HVF) to the pEW of the photospheric velocity feature (PVF). Briefly, we first normalise the Ca NIR feature using a linear pseudo-continuum fit. We then fit the Ca NIR feature with two Gaussians in *velocity space* with velocity centres, widths, and absorption depths fitted with a Python `mpfit` routine. Each component in velocity space corresponds to a triplet in wavelength space, and we set the absorption depth of each component equal to each other (i.e. the optically thick limit). As in Childress et al. (2014a), we require the photospheric velocity component to have a velocity centre within 20% of the value derived for the Si 6355Å feature, though in most cases the results are the same if this requirement is removed.

In Figure 9 we plot the measured high velocity feature strength (R_{HVF}) versus the silicon absorption strength ratio R_{Si} . For illustrative purposes, we also show the scale of light curve decline rate Δm_{15} corresponding to the plotted range of R_{Si} using the above relation. A representative errorbar for Δm_{15} from the above relation and a typical R_{HVF} errorbar are shown in the figure.

Figure 9 demonstrates a tendency for SNe Ia with strong HVFs to also have low values of R_{Si} and thus broad light curves (low Δm_{15}). This correlation of HVFs with SN Ia light curve width was first observed by Maguire et al. (2012) in composite high-redshift SN Ia spectra, and subsequently confirmed by numerous studies of low-redshift SNe Ia (Childress et al. 2014a;

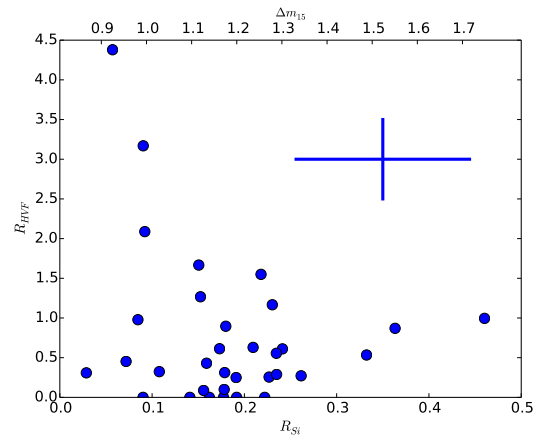


Figure 9. Strength of the high-velocity features (HVF) in the Ca II NIR triplet – using the quantity R_{HVF} as defined by Childress et al. (2014a) – plotted against the Si II absorption strength ratio R_{Si} defined by Nugent et al. (1995). On the top axis we show the rough equivalent light curve decline rate Δm_{15} values corresponding to the range of R_{Si} values. The crosshair in the upper right represents the characteristic errors in measurement of R_{HVF} (typically 20%, plotted here for the larger values of R_{HVF}) and the error in Δm_{15} when converted from R_{Si} .

Maguire et al. 2014; Pan et al. 2015; Silverman et al. 2015; Zhao et al. 2015). Our results support these studies with spectra alone.

4.2 Narrow sodium absorption features in SN Ia spectra

A great advantage of the higher resolution of WiFeS (compared to many spectrographs deployed for other SN spectroscopy surveys) is the ability to detect narrow absorption features, particularly the Na I doublet at $\lambda\lambda 5890/5896\text{\AA}$. This feature has a long history of being used to infer the presence of foreground dust in SNe Ia (Barbon et al. 1990; Turatto et al. 2003; Poznanski et al. 2011, 2012; Phillips et al. 2013). Earlier works attempted to derive correlations between SN Ia colors and sodium absorption strength (i.e. the absorption equivalent width), but Poznanski et al. (2011) showed sodium to be a poor indicator of SN Ia reddening. Phillips et al. (2013) refined this result by showing that SN Ia reddening exhibits a strong correlation with absorption strength of the diffuse interstellar bands (found exclusively in the interstellar medium) but some SNe Ia have an excess of sodium absorption that does *not* coincide with associated reddening of the SN. Thus sodium features in SNe Ia remain instructive but should be considered with a measure of caution.

Recently, velocities of sodium absorption features in SN Ia spectra have been used as a diagnostic of circumstellar material (CSM), including cases of some SNe Ia (Patat et al. 2007; Simon et al. 2009) where the sodium absorption features exhibit variability (though most do not – see Sternberg et al. 2014), indicating SN-CSM interaction. More recently, a statistical analysis of the velocity distribution of sodium features in SNe Ia by Sternberg et al. (2011) found an excess of SNe Ia with blueshifted sodium features, indicating that a fraction of SNe Ia explode inside an expanding shell of material that was presumably shed by the SN Ia progenitor system prior to explosion. Maguire et al. (2013) extended this work to show that the excess of SNe Ia with blueshifted sodium absorption was populated predominantly by the more luminous SNe Ia with slow declining light curves (i.e. high “stretch”).

We thus searched for the presence of sodium absorption features in our sample of SN Ia spectra. For most SNe Ia (13) this was done with the lower resolution (R3000) observations of the SN at maximum light. For six SNe Ia, we also had a higher resolution (R7000) observation of the SN at maximum light. In a few instances this observation was triggered by the presence of strong reddening being reported in the SN classification announcement. For the other instances, we obtained both a low-resolution (R3000) and high-resolution (R7000) spectrum in the red while obtaining a longer exposure blue (B3000) spectrum during nights near full moon when the blue sky background was exceptionally high.

We fitted the sodium doublet absorption profile as follows. First the spectrum was normalized to the local continuum by fitting a quadratic to the SN flux between 10–25Å redward or blueward of the doublet centre (5893Å). The absorption profile was fitted as two Gaussians with rest wavelengths set by the doublet wavelengths but with unknown (common) velocity shift and velocity width and (independent) absorption depths. This was done with an `mpfit` routine in Python, which accounts for variable covariances and returns the appropriate fit values and uncertainties. We show representative examples for fits to data from both gratings in Figure 10. The outcomes for our sodium profile fits are presented in Table 7 in Appendix A, and comprise 6 successful fits for targets with R7000 spectra, and 13 for R3000 spectra.

The primary quantity we wanted to measure from the sodium absorption feature was its velocity with respect to the local standard of rest at the SN site. The default local rest velocity was initially set to be the systemic velocity of the SN host galaxy. In some cases we detected clear nebular emission lines at the SN site present in the SN spectrum – for these cases the local rest velocity (i.e., the rotational velocity of the host galaxy at the site of the SN) was measured from the H α emission line.

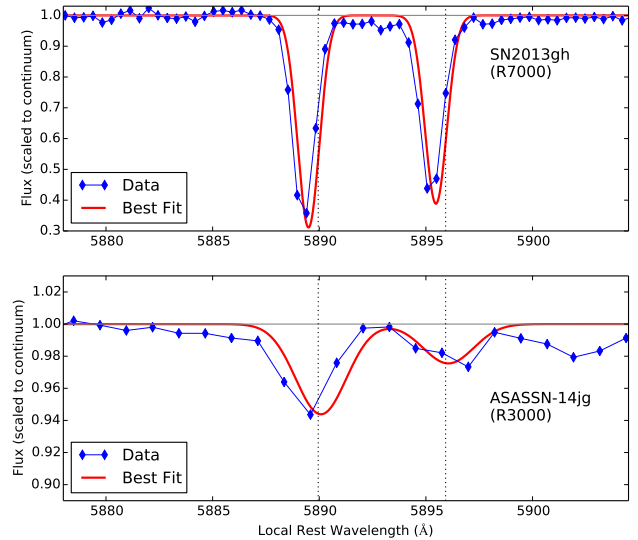


Figure 10. Sodium absorption fit examples for both the R7000 (top) and R3000 (bottom) gratings. Data (which have been normalised to the local continuum fit) are shown as blue diamonds while the best fit absorption profile is shown as the solid red curve. For reference, we also mark the continuum level (horizontal black line at value 1.00) and the rest wavelengths of the sodium doublet (vertical dotted grey lines).

In two cases (SN 2014ao and ASASSN-14jg) no local H α emission was present in the SN spectrum, and the SN sodium velocity differed from the host systemic velocity by more than 100 km s $^{-1}$. To obtain the true local rest velocities for these two SNe Ia, we took advantage of the integral-field data provided by WiFeS, which allows us to measure host galaxy properties (such as velocity) over a broad field of view.

We illustrate this for SN 2014ao in Figure 11: the WiFeS field of view extends from the host galaxy core to the outer edge of its spiral arms in the direction of the SN. We were able to extract the velocity of an H II region along the SN-host axis and found its velocity differed significantly from that of the host core. As galaxy velocity curves tend to flatten at large radii, we use the H II region velocity as the local rest velocity of SN 2014ao – a value much closer to the measured sodium absorption velocity.

With the final sodium absorption velocities for our sample, we can inspect the relationship between sodium velocity and other spectroscopic properties of our SN Ia sample. In Figure 12 we plot the silicon absorption ratio (R_{Si}), the HVF absorption strength (R_{HVF}), and the absorption strength (i.e. equivalent width) of sodium itself against the velocity of the sodium absorption feature. Based on results of Maguire et al. (2013), we would

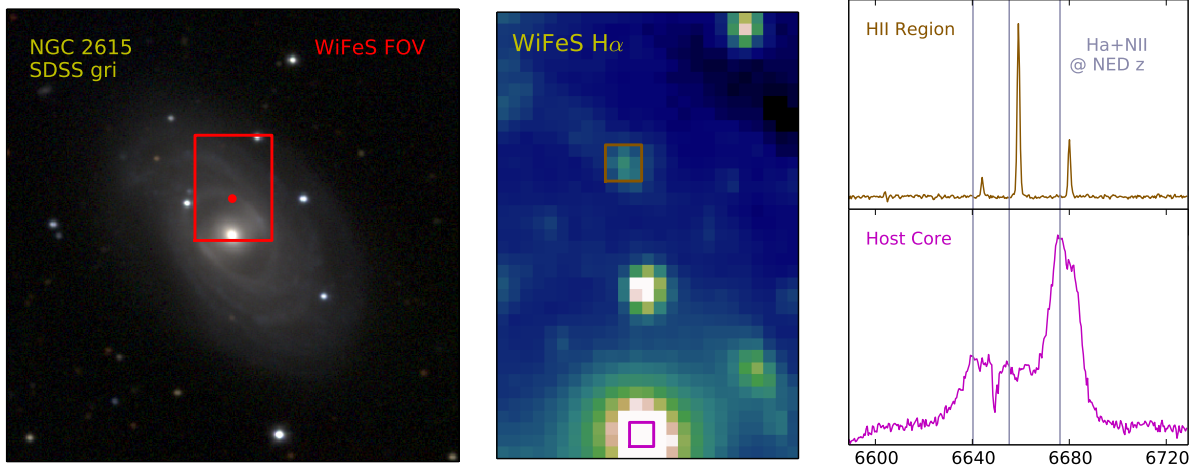


Figure 11. Determination of the local velocity for SN 2014ao in NGC 2615 with WiFeS. Left: SDSS (York et al. 2000) *gri* color composite – created with SWARP (Bertin et al. 2002) and STIFF (Bertin 2012) – with the WiFeS field of view (red rectangle) and SN location (red dot) highlighted. Middle: Image of the SN 2014ao WiFeS data cube in the isolated wavelength range within $\pm 6 \text{ \AA}$ (i.e. $\pm 300 \text{ km s}^{-1}$) of the wavelength of $\text{H}\alpha$ at the published redshift of NGC 2615, with host core (purple square) and nearby H II region (brown square) highlighted – the SN is the bright object near the centre. Right: Extracted WiFeS spectra of the nearby H II region (top) and host core (bottom) near the $\text{H}\alpha + \text{NII}$ emission line group, with the expected location of those lines at the published redshift of NGC 2615 ($z=0.014083$ Theureau et al. 1998a) shown as the vertical grey lines.

expect SNe Ia with low R_{Si} and high R_{HVF} values (the high stretch, slow declining SNe Ia) to have a slight excess of blueshifted sodium absorption. Our sample size here is too small (and not well-selected) to make any robust statement about such preferences. However we note that this analysis was not the explicit objective of our observations, but instead was a supplemental outcome facilitated by the nature of the WiFeS data.

Thus WiFeS is an excellent instrument for measuring sodium absorption in SNe Ia, a key observable for investigating SN Ia progenitor systems. This is particularly true for observations taken with the R7000 grating, which provides sodium velocity uncertainties of order a few km s^{-1} , thus enabling a robust classification of the SN as being “blueshifted” or “redshifted”. More importantly, perhaps, is the capability of WiFeS to observe a wide field of view around the SN. This enables a measurement of the local systemic velocity at the SN location, even in cases where emission from the host galaxy is weak at the SN location itself.

4.3 Spectroscopic evolution of SN 2012dn

The SN with the greatest number of spectroscopic epochs in AWSNAP is SN 2012dn, and we show its AWSNAP spectroscopic time series in Figure 13. SN 2012dn was a spectroscopically peculiar SN Ia

whose photometric and spectroscopic evolution was studied extensively by and Chakradhari et al. (2014) – they found it to be similar to the candidate “super-Chandrasekhar” (hereafter super-Chandra) SN Ia SN 2006gz (Hicken et al. 2007). We comment on only a few additional outcomes from the AWSNAP data, but refer readers to Chakradhari et al. (2014) and Parrent et al. (2016) for a thorough discussion of this interesting object.

We obtained a very high signal-to-noise spectrum of SN 2012dn at phase +91 days (with respect to the date of maximum light 2012 July 24, as determined by Chakradhari et al. 2014). At this epoch the SN is beginning to enter the nebular phase when the ejecta become optically thin, revealing emission from the iron group elements (IGEs) near the centre of the SN. Spectra at these epochs provide an excellent diagnostic of the nucleosynthetic products of the SN explosion. In Figure 14 we present our +91 day spectrum of SN 2012dn compared to very late spectra of other candidate super-Chandra SNe Ia SN 2007if (Scalzo et al. 2010; Yuan et al. 2010; Taubenberger et al. 2013) and SN 2009dc (Silverman et al. 2011; Taubenberger et al. 2011; Yamanaka et al. 2009; Tanaka et al. 2010; Hachinger et al. 2012; Kamiya et al. 2012; Taubenberger et al. 2013), as well as the gold standard normal SN Ia SN 2011fe

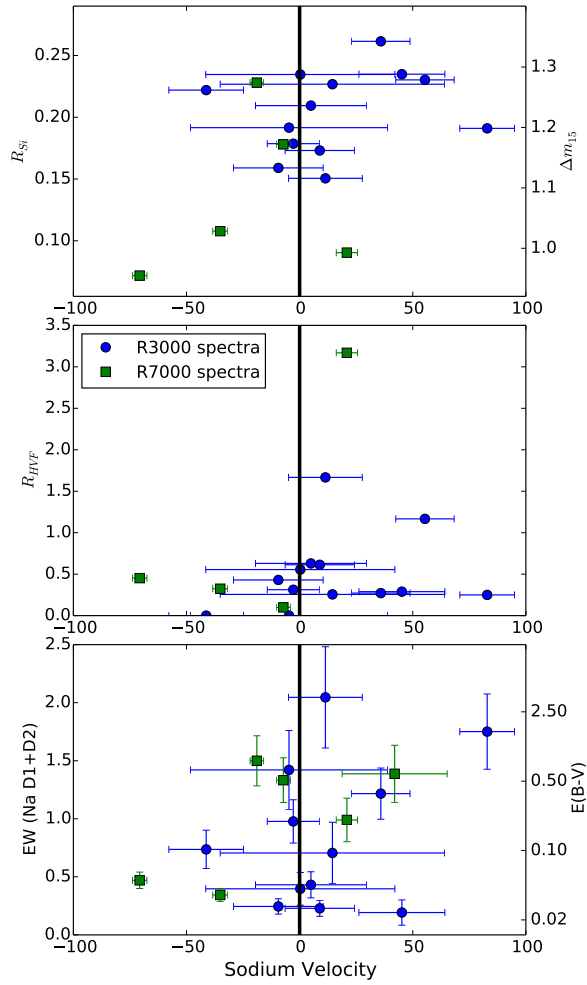


Figure 12. Top: Silicon absorption ratio R_{Si} plotted against velocity centre of the narrow sodium absorption feature (as in Figure 9 we show the corresponding values of Δm_{15} , though note the smaller range). Middle: HVF strength (R_{HVF}) plotted against sodium absorption velocity. Bottom: Absorption equivalent width of the combined D1+D2 sodium lines plotted against sodium absorption velocity. On the right axis of this panel we use the relation of Poznanski et al. (2012) to show the reddening values $E(B - V)$ corresponding to the measured sodium equivalent widths if the absorption arises solely from the ISM – though this is unlikely to be true for all SNe Ia (Poznanski et al. 2011; Phillips et al. 2013, – see discussion in text). In all panels, higher resolution observations with the R7000 grating are displayed as green squares, while lower resolution R3000 observations are shown as blue circles.

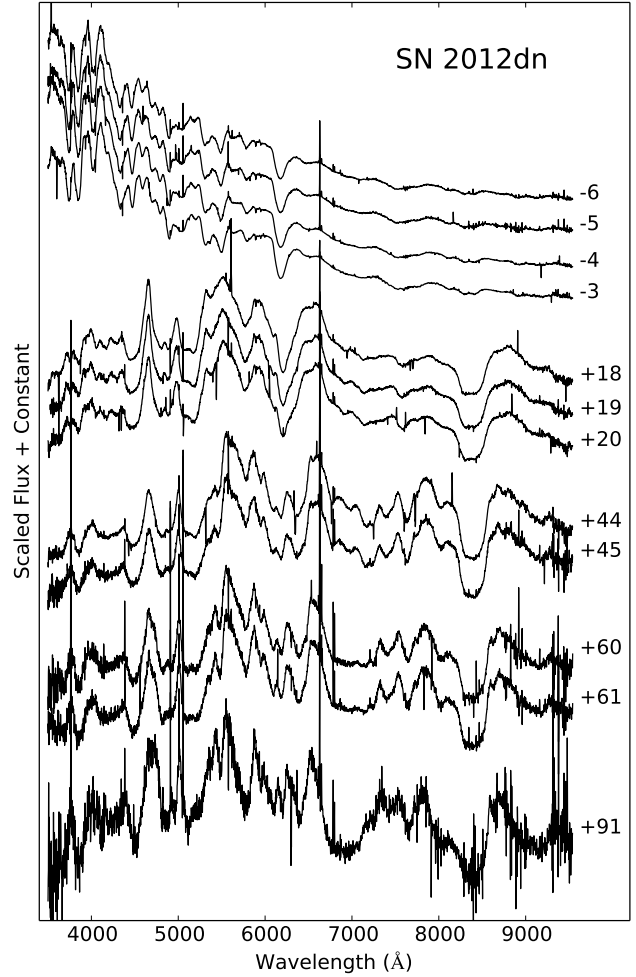


Figure 13. AWSNAP time series of SN 2012dn, labeled by phase with respect to the date of maximum light (2012 July 24, as determined by Chakradhari et al. 2014). Note these observations come from the first semester of AWSNAP when observing time was allocated in multi-night blocks separated sometimes by a month or more.

(Nugent et al. 2011; Li et al. 2011a; Parrent et al. 2012; Pereira et al. 2013).

This comparison clearly reveals a strong spectroscopic similarity between SN 2012dn and the candidate super-Chandrasekhar SNe Ia, and a distinct dissimilarity with SN 2011fe. Perhaps most prominent is the weaker Fe III line complex at ~ 4700 Å for the super-Chandra SNe Ia compared to SN 2011fe. This discrepancy is also evident in fully nebular spectra of super-Chandra SNe Ia at ~ 1 year past maximum light, as discussed by Taubenberger et al. (2013). This indicates that the ionisation state of the super-Chandra SNe Ia at these phases is different from normal SNe Ia – whether

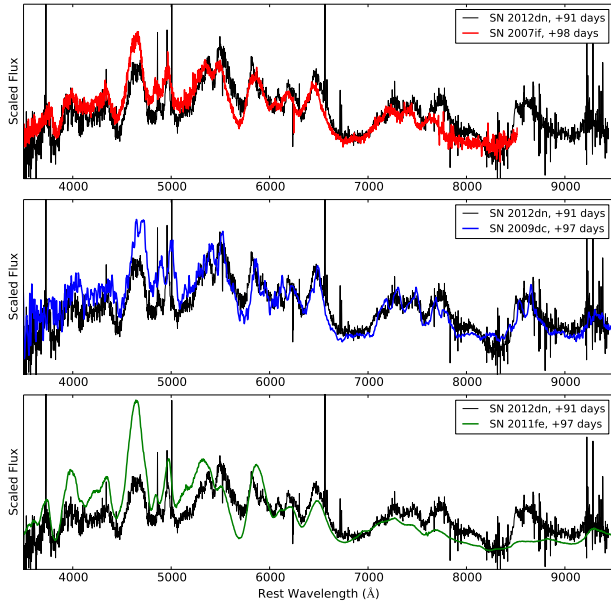


Figure 14. SN 2012dn at its latest AWSNAP epoch (+91 days on 2012 Oct 23) compared to other candidate super-Chandra SNe Ia SN 2007if at +98 days (top panel, from Silverman et al. 2011) and SN 2009dc at +97 days (middle panel, from Taubenberger et al. 2011), as well as the normal SN 2011fe (bottom panel, from Pereira et al. 2013).

the diminished Fe III emission arises from a higher or lower average ionisation state remains uncertain.

Additionally, the velocity profile of the emission features in the super-Chandra SNe Ia exhibits a marked difference to that of SN 2011fe (and other normal SNe Ia). The normal SN Ia profile appears very Gaussian (and indeed is generally well fit by a Gaussian profile – Childress et al. 2015), while the super-Chandra velocity profile appears sharper at the centre. This is particularly evident for the line features at ~ 5900 Å and ~ 6300 Å, which at these epochs are dominated by Co III. Further spectral modeling of this and other late-phase super-Chandra spectra may reveal important insights into the structure and composition of the super-Chandra ejecta.

Finally, the high resolution of WiFeS reveals narrow emission lines from the host galaxy of SN 2012dn. We isolated the narrow host galaxy lines using the longest exposure of SN 2012dn, the late-phase observation of 2012 Oct 23 (+91 days). We fit a simple linear “continuum” near each emission line by fitting a line to the SN spectrum between 5 and 15 Å away from the line centre on both the blue and red sides of the line. We illustrate this technique and present the SN-subtracted emission features in Figure 15.

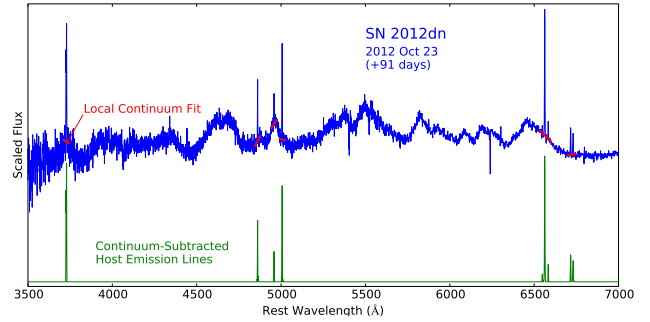


Figure 15. Extraction of host galaxy emission line flux (green) from late SN 2012dn spectrum (blue) using simple linear continuum fits (red).

Table 3 SN 2012dn Local Emission Line Fluxes

Line	$F(\lambda)/F(H\beta)$ (raw) ^a	$F(\lambda)/F(H\beta)$ (de-reddened) ^b
[O II] $\lambda\lambda 3727, 3730$	3.61 ± 0.24	4.33 ± 0.29
H β	1.00 ± 0.10	1.00 ± 0.10
[O III] $\lambda 4959$	0.45 ± 0.09	0.44 ± 0.09
[O III] $\lambda 5007$	1.64 ± 0.10	1.60 ± 0.10
H α	3.40 ± 0.07	2.87 ± 0.06
[N II] $\lambda 6548$	0.06 ± 0.06	0.05 ± 0.05
[N II] $\lambda 6584$	0.37 ± 0.06	0.31 ± 0.05
[S II] $\lambda 6717$	0.71 ± 0.06	0.59 ± 0.05
[S II] $\lambda 6731$	0.58 ± 0.06	0.48 ± 0.05

^a Observer frame fluxes, scaled to H β .

^b Dereddened using Balmer decrement reddening of $E(B - V) = 0.17$ so that $F(H\beta) = F(H\alpha)/2.87$ with a CCM reddening law, and scaled to the de-reddened flux of H β .

In Table 3 we present the measured emission fluxes and errors for the major galaxy emission lines, all of which have been scaled by the observed flux in the H β line. By comparing the observed ratio of the H α and H β lines to its expected value of 2.87 (the Balmer decrement Osterbrock & Ferland 2006), we can determine the amount of reddening in the H II regions giving rise to the host emission lines. We use the Cardelli et al. (1989) to find a host reddening of $E(B - V) = 0.17 \pm 0.10$, a value remarkably similar to the SN reddening of $E(B - V) = 0.18$ (Milky Way plus host) determined by Chakradhari et al. (2014). We correct the host emission line fluxes for the value $E(B - V) = 0.17$ and report the corrected values (which we also re-scale to the dereddened H β flux) in Table 3.

With the de-reddened host galaxy emission line fluxes, we calculate a gas-phase metallicity at the site of SN 2012dn. The N2 method of Pettini & Pagel (2004, hereafter PP04) yields $12 + \log(O/H) = 8.29 \pm 0.04$, while the O3N2 method of PP04 yields $12 + \log(O/H) = 8.35 \pm 0.03$. The former value is remark-

ably close to the estimated site metallicity for SN 2006gz of $12 + \log(O/H) = 8.26$ calculated by Khan et al. (2011) using the same metallicity method. If we convert the O3N2 value to the Tremonti et al. (2004) scale using the formulae of Kewley & Ellison (2008) as was done in Childress et al. (2011), we measure $12 + \log(O/H)_{T04} = 8.51 \pm 0.04$.

Comparing the above values to the solar oxygen abundance of $12 + \log(O/H)_{\odot} = 8.69$ (Asplund et al. 2009) we find the site metallicity for SN 2012dn is in the range 40-65% solar, depending on the chosen metallicity calibration. This sub-solar metallicity value is consistent with the previously reported trend for super-Chandra SNe Ia to prefer low metallicity environments (Taubenberger et al. 2011; Childress et al. 2011; Khan et al. 2011).

5 Conclusions

This work marks the primary data release for the ANU WiFeS SuperNova Program (AWSNAP), comprising 357 distinct spectra of 175 unique supernovae. These data were collected using the Wide Field Spectrograph (WiFeS) on the ANU 2.3m telescope during 82 nights of observing over a three-year period from mid-2012 to mid-2015.

The AWSNAP spectroscopy sample is comparable in size to other SN spectra data releases, and its composition of SN types is roughly in line with expectations for a magnitude-limited SN search. The phase coverage of the AWSNAP SN Ia sample is comparable to other published SN Ia spectroscopy datasets (for SNe Ia with multiple epochs of observation), with the inclusion of more SNe Ia with a single observation (i.e., classification spectra only).

We presented some analyses of the AWSNAP SN Ia sample, including some results uniquely enabled by the fine wavelength resolution available with WiFeS. We measured broad absorption features in SN Ia spectra at maximum light, including the ratio of silicon absorption features R_{Si} and the strength of high velocity features R_{HVF} . Additionally, we measured the strength and velocity of narrow sodium absorption features, including some cases where the integral-field nature of the instrument allowed us to measure the local systemic velocity within the SN host galaxy. Some expected feature trends, such as a correlation between R_{HVF} and R_{Si} , were recovered in our data set. The nature of sodium absorption in our sample was limited by small number statistics. Finally, we presented our observations of the candidate super-Chandrasekhar SN Ia SN 2012dn, and used narrow host galaxy emission features to show the SN site exhibits sub-solar metallicity.

The WiFeS instrument presents several unique advantages for the study of transients, particularly owing to its comparatively narrow velocity resolution ($\sigma_v \sim$

45 km s⁻¹). It has previously been employed in the study of SNe with strong narrow emission features such as SN 2009ip (Fraser et al. 2013, 2015), SN 2012ca (Inserra et al. 2014, 2016), and SN 2013fc (Kangas et al. 2016). Here we also demonstrated that the fine velocity resolution allows for the measurement of narrow *absorption* features, particularly sodium absorption in SNe Ia. The higher resolution of WiFeS also frequently revealed narrow host galaxy emission features at the site of the SN, which can at times be used to determine a SN site metallicity (as we showed for SN 2012dn). Finally, the integral field nature of WiFeS allowed us to measure the local host galaxy rotational velocity at the site of several SNe, even when there was no emission directly at the SN location. Thus WiFeS is an instrument well-suited for not only standard SN spectroscopic observations, but also a unique suite of capabilities not commonly found in transient followup instruments.

Acknowledgements

We are very grateful for the excellent technical support staff for the ANU 2.3m telescope and the WiFeS instrument: Peter Verwayen, Ian Adams, Peter Small, Ian Price, Peter Young, and Jon Nielsen. We thank the ANU telescope time allocation committee who continue to support the observations presented herein. We also thank Julie Banfield, Michael Ireland, Stefan Keller, Lisa Kewley, Jeremy Mould, Chris Owen, Aaron Rizzuto, Dary Ruiz, and Tian-Tian Yuan for additional observations.

This research was conducted by the Australian Research Council Centre of Excellence for All-sky Astrophysics (CAASTRO), through project number CE110001020. IRS was supported by Australian Research Council Laureate Grant FL0992131. This research has made use of the NASA/IPAC Extragalactic Database (NED) which is operated by the Jet Propulsion Laboratory, California Institute of Technology, under contract with the National Aeronautics and Space Administration. This research has made use of NASA's Astrophysics Data System (ADS).

REFERENCES

- Aldering, G., et al. 2002, in Society of Photo-Optical Instrumentation Engineers (SPIE) Conference Series, Vol. 4836, Survey and Other Telescope Technologies and Discoveries, ed. J. A. Tyson & S. Wolff, 61–72
- Asplund, M., Grevesse, N., Sauval, A. J., & Scott, P. 2009, *ARA&A*, 47, 481
- Bailey, S., et al. 2009, *A&A*, 500, L17
- Baltay, C., et al. 2013, *PASP*, 125, 683
- Barbon, R., Benetti, S., Rosino, L., Cappellaro, E., & Turatto, M. 1990, *A&A*, 237, 79

- Benetti, S., et al. 2005, *ApJ*, 623, 1011
- Bertin, E. 2012, in *Astronomical Society of the Pacific Conference Series*, Vol. 461, *Astronomical Data Analysis Software and Systems XXI*, ed. P. Ballester, D. Egret, & N. P. F. Lorente, 263
- Bertin, E., Mellier, Y., Radovich, M., Missonnier, G., Didelon, P., & Morin, B. 2002, in *Astronomical Society of the Pacific Conference Series*, Vol. 281, *Astronomical Data Analysis Software and Systems XI*, ed. D. A. Bohlender, D. Durand, & T. H. Handley, 228
- Bessell, M. S. 1999, *PASP*, 111, 1426
- Bianco, F. B., et al. 2014, *ApJS*, 213, 19
- Blagorodnova, N., Kopusov, S. E., Wyrzykowski, L., Irwin, M., & Walton, N. A. 2014, *MNRAS*, 442, 327
- Blagorodnova, N., Van Velzen, S., Harrison, D. L., Kopusov, S., Mattila, S., Campbell, H., Walton, N. A., & Wyrzykowski, L. 2016, *MNRAS*, 455, 603
- Blondin, S., Mandel, K. S., & Kirshner, R. P. 2011, *A&A*, 526, A81
- Blondin, S., & Tonry, J. L. 2007, *ApJ*, 666, 1024
- Blondin, S., et al. 2012, *AJ*, 143, 126
- Bongard, S., Baron, E., Smadja, G., Branch, D., & Hauschildt, P. H. 2006, *ApJ*, 647, 513
- . 2008, *ApJ*, 687, 456
- Branch, D., Dang, L. C., & Baron, E. 2009, *PASP*, 121, 238
- Branch, D., et al. 2006, *PASP*, 118, 560
- Bronder, T. J., et al. 2008, *A&A*, 477, 717
- Brown, T. M., et al. 2013, *PASP*, 125, 1031
- Cardelli, J. A., Clayton, G. C., & Mathis, J. S. 1989, *ApJ*, 345, 245
- Chakradhari, N. K., Sahu, D. K., Srivastav, S., & Anupama, G. C. 2014, *MNRAS*, 443, 1663
- Childress, M., et al. 2011, *ApJ*, 733, 3
- Childress, M. J., Filippenko, A. V., Ganeshalingam, M., & Schmidt, B. P. 2014a, *MNRAS*, 437, 338
- Childress, M. J., Vogt, F. P. A., Nielsen, J., & Sharp, R. G. 2014b, *Ap&SS*, 349, 617
- Childress, M. J., et al. 2015, *MNRAS*, 454, 3816
- Cortese, L., et al. 2008, *MNRAS*, 383, 1519
- da Costa, L. N., Pellegrini, P. S., Davis, M., Meiksin, A., Sargent, W. L. W., & Tonry, J. L. 1991, *ApJS*, 75, 935
- Donzelli, C. J., & Pastoriza, M. G. 2000, *AJ*, 120, 189
- Dopita, M., Hart, J., McGregor, P., Oates, P., Bloxham, G., & Jones, D. 2007, *Ap&SS*, 310, 255
- Dopita, M., et al. 2010, *Ap&SS*, 327, 245
- Drake, A. J., et al. 2009, *ApJ*, 696, 870
- Filippenko, A. V. 1997, *ARA&A*, 35, 309
- Filippenko, A. V., et al. 1992a, *ApJL*, 384, L15
- . 1992b, *AJ*, 104, 1543
- Folatelli, G., et al. 2013, *ApJ*, 773, 53
- Foley, R. J., et al. 2013, *ApJ*, 767, 57
- Fraser, M., et al. 2013, *MNRAS*, 433, 1312
- . 2015, *MNRAS*, 453, 3886
- Ganeshalingam, M., et al. 2010, *ApJS*, 190, 418
- Graur, O., Bianco, F. B., Modjaz, M., Maoz, D., Shivers, I., Filippenko, A. V., & Li, W. 2015, *ArXiv e-prints*
- Grogin, N. A., Geller, M. J., & Huchra, J. P. 1998, *ApJS*, 119, 277
- Hachinger, S., Mazzali, P. A., & Benetti, S. 2006, *MNRAS*, 370, 299
- Hachinger, S., Mazzali, P. A., Tanaka, M., Hillebrandt, W., & Benetti, S. 2008, *MNRAS*, 389, 1087
- Hachinger, S., Mazzali, P. A., Taubenberger, S., Fink, M., Pakmor, R., Hillebrandt, W., & Seitenzahl, I. R. 2012, *MNRAS*, 427, 2057
- Hatano, K., Branch, D., Lentz, E. J., Baron, E., Filippenko, A. V., & Garnavich, P. M. 2000, *ApJL*, 543, L49
- Hicken, M., Garnavich, P. M., Prieto, J. L., Blondin, S., DePoy, D. L., Kirshner, R. P., & Parrent, J. 2007, *ApJL*, 669, L17
- Inserra, C., et al. 2013, *ApJ*, 770, 128
- . 2014, *MNRAS*, 437, L51
- . 2016, *MNRAS*, 459, 2721
- Kaiser, N., et al. 2010, in *Society of Photo-Optical Instrumentation Engineers (SPIE) Conference Series*, Vol. 7733, *Ground-based and Airborne Telescopes III*, 0
- Kamiya, Y., Tanaka, M., Nomoto, K., Blinnikov, S. I., Sorokina, E. I., & Suzuki, T. 2012, *ApJ*, 756, 191
- Kangas, T., et al. 2016, *MNRAS*, 456, 323
- Keller, S. C., et al. 2007, *PASA*, 24, 1
- Kelson, D. D. 2003, *PASP*, 115, 688
- Kewley, L. J., & Ellison, S. L. 2008, *ApJ*, 681, 1183
- Khan, R., Stanek, K. Z., Stoll, R., & Prieto, J. L. 2011, *ArXiv e-prints*
- Klotz, A., Boer, M., Atteia, J.-L., Gendre, B., Le Borgne, J.-F., Frappa, E., Vachier, F., & Berthier, J. 2013, *The Messenger*, 151, 6
- Law, N. M., et al. 2009, *PASP*, 121, 1395
- Li, W., et al. 2011a, *Nature*, 480, 348
- . 2011b, *MNRAS*, 412, 1441
- Lipunov, V. M., et al. 2004, *Astronomische Nachrichten*, 325, 580
- Liu, Y.-Q., Modjaz, M., Bianco, F. B., & Graur, O. 2015, *ArXiv e-prints*
- Maguire, K., et al. 2012, *MNRAS*, 426, 2359
- . 2013, *MNRAS*, 436, 222
- . 2014, *MNRAS*, 444, 3258
- Matheson, T., et al. 2008, *AJ*, 135, 1598
- Modjaz, M., et al. 2014, *AJ*, 147, 99
- Nugent, P., Phillips, M., Baron, E., Branch, D., & Hauschildt, P. 1995, *ApJL*, 455, L147

- Nugent, P. E., et al. 2011, *Nature*, 480, 344
- Ogando, R. L. C., Maia, M. A. G., Pellegrini, P. S., & da Costa, L. N. 2008, *AJ*, 135, 2424
- Oke, J. B. 1990, *AJ*, 99, 1621
- Osterbrock, D. E., & Ferland, G. J. 2006, *Astrophysics of gaseous nebulae and active galactic nuclei*, ed. Osterbrock, D. E. & Ferland, G. J.
- Pan, Y.-C., Sullivan, M., Maguire, K., Gal-Yam, A., Hook, I. M., Howell, D. A., Nugent, P. E., & Mazzali, P. A. 2015, *MNRAS*, 446, 354
- Parrent, J. T., et al. 2012, *ApJL*, 752, L26
- . 2016, *MNRAS*, 457, 3702
- Patat, F., et al. 2007, *Science*, 317, 924
- Pereira, R., et al. 2013, *A&A*, 554, A27
- Pettini, M., & Pagel, B. E. J. 2004, *MNRAS*, 348, L59
- Phillips, M. M., et al. 2013, *ApJ*, 779, 38
- Pignata, G., et al. 2009, in *American Institute of Physics Conference Series*, Vol. 1111, American Institute of Physics Conference Series, ed. G. Giobbi, A. Tornambe, G. Raimondo, M. Limongi, L. A. Antonelli, N. Menci, & E. Brocato, 551–554
- Planck Collaboration et al. 2011, *A&A*, 536, A1
- Poznanski, D., Ganeshalingam, M., Silverman, J. M., & Filippenko, A. V. 2011, *MNRAS*, 415, L81
- Poznanski, D., Prochaska, J. X., & Bloom, J. S. 2012, *MNRAS*, 426, 1465
- Quimby, R. M. 2006, PhD thesis, The University of Texas at Austin
- Rau, A., et al. 2009, *PASP*, 121, 1334
- Salim, S., et al. 2007, *ApJS*, 173, 267
- Sandage, A., & Tammann, G. A. 1981, in *Carnegie Inst. of Washington*, Publ. 635; Vol. 0; Page 0, Vol. 0
- Scalzo, R., et al. 2012, *ApJ*, 757, 12
- Scalzo, R. A., et al. 2010, *ApJ*, 713, 1073
- Shappee, B. J., et al. 2014, *ApJ*, 788, 48
- Silverman, J. M., Ganeshalingam, M., Li, W., & Filippenko, A. V. 2012a, *MNRAS*, 425, 1889
- Silverman, J. M., Ganeshalingam, M., Li, W., Filippenko, A. V., Miller, A. A., & Poznanski, D. 2011, *MNRAS*, 410, 585
- Silverman, J. M., Kong, J. J., & Filippenko, A. V. 2012b, *MNRAS*, 425, 1819
- Silverman, J. M., Vinkó, J., Marion, G. H., Wheeler, J. C., Barna, B., Szalai, T., Mulligan, B. W., & Filippenko, A. V. 2015, *MNRAS*, 451, 1973
- Silverman, J. M., et al. 2012c, *MNRAS*, 425, 1789
- Simon, J. D., et al. 2009, *ApJ*, 702, 1157
- Smartt, S. J., et al. 2015, *A&A*, 579, A40
- Sternberg, A., et al. 2011, *Science*, 333, 856
- . 2014, *MNRAS*, 443, 1849
- Stritzinger, M., Suntzeff, N. B., Hamuy, M., Challis, P., Demarco, R., Germany, L., & Soderberg, A. M. 2005, *PASP*, 117, 810
- Tanaka, M., et al. 2010, *ApJ*, 714, 1209
- Taubenberger, S., et al. 2011, *MNRAS*, 412, 2735
- . 2013, *MNRAS*, 432, 3117
- Theureau, G., Bottinelli, L., Coudreau-Durand, N., Gouguenheim, L., Hallet, N., Loulergue, M., Patrel, G., & Teerikorpi, P. 1998a, *A&AS*, 130, 333
- . 1998b, *A&AS*, 130, 333
- Tomasella, L., et al. 2014, *Astronomische Nachrichten*, 335, 841
- Tremonti, C. A., et al. 2004, *ApJ*, 613, 898
- Turatto, M., Benetti, S., & Cappellaro, E. 2003, in *From Twilight to Highlight: The Physics of Supernovae*, ed. W. Hillebrandt & B. Leibundgut, 200
- van Dokkum, P. G. 2001, *PASP*, 113, 1420
- Wang, X., et al. 2009, *ApJL*, 699, L139
- Wyrzykowski, L., Hodgkin, S., Blogrodnova, N., Koposov, S., & Burgon, R. 2012, *ArXiv e-prints*
- Wyrzykowski, L., et al. 2014, *ACTA*, 64, 197
- Yamanaka, M., et al. 2009, *ApJL*, 707, L118
- Yaron, O., & Gal-Yam, A. 2012, *PASP*, 124, 668
- York, D. G., et al. 2000, *AJ*, 120, 1579
- Yuan, F. 2010, PhD thesis, University of Michigan
- Yuan, F., et al. 2010, *ApJ*, 715, 1338
- Zhao, X., et al. 2015, *ApJS*, 220, 20

Appendix A1: Target and Observation Details

In this Appendix we present the observational metadata for the AWSNAP data release, as well as sodium fit results and host (or local) redshifts used in the sodium fitting.

AWSNAP targets: Table 4 presents the discovery and classification details for the full list of 175 objects featured in the AWSNAP DR1 data release. We list the discovery location and date, as well as discovery reference and group that discovered the transient. Note the discovery references are typically either Astronomer’s Telegrams (ATel’s, denoted as, e.g., “A1234”) or telegrams from the Central Bureau for Electronic Telegrams (CBET’s, denoted as, e.g., “C1234”), though occasionally a separate discovery notice was not issued – in these cases typically the webpage of the discovering group was cited in the classification reference. Classification references are given with similar notation, listed along with with classification date, quoted supernova type and phase from the classification, as well as the redshift listed in the classification.

Table 4. All AWSNAP Targets

SN	Discovery			Classification			Phase ^d				
	RA	DEC	Ref. ^a	Date	Group ^b	Ref.		Date	Group ^c	SN Type	Redshift
SN 2009ip	22:23:08.1	-28:56:35	A4334	20120724	CRTS	A4338	20120826	Foley	SNIIn	0.005944	(unk)
SN 2012ea	18:41:06.5	-41:47:38	C3101	20120426	Parker	A4076	20120429	PESSTO	SNIIn	0.019000	(unk)
SN 2012dj	23:14:47.2	-43:36:22	C3167	20120702	Parker	C3167	20120706	Parrent	SNb/c	0.005324	+0
SN 2012dm	20:23:36.3	-28:16:43	C3174	20120708	Parker	A4253	20120712	SNF	SNIa	0.010187	-10
SN 2012dt	00:56:38.1	-09:53:59	C3188	20120718	Parker	A4269	20120721	PTF	SNI	0.018900	+9
SN 2012dy	21:18:49.5	-57:38:42	C3197	20120804	Bock	C3197	20120805	Milisavljevic	SNI	0.010300	(young)
SN 2012ec	02:45:59.9	-07:34:15	C3201	20120811	Monard	A4306	20120812	AWSNAP	SNI	0.004693	(young)
SN 2012eq	01:00:14.5	-30:48:26	C3223	20120827	CRTS	A4362	20120907	PESSTO	SNIa	0.032230	+45
SN 2012eu	03:13:04.2	-08:23:24	C3231	20120827	CRTS	C3231	20120904	Yang	SNIa	0.030000	+30
SN 2012fr	03:33:37.1	-36:07:28	A4523	20121027	TAROT	A4525	20121028	AWSNAP	SNIa	0.005400	-11

Note. — Abbreviated version – full version of this table included in arXiv package.

^a Notation: A1234 \equiv ATel # 1234; C1234 \equiv CBET # 1234; CTOCP \equiv CBET Transient Object Confirmation Page; objects newly classified here denoted as (NEW); all others refer to transient announcement webpages for stated discovery group(s).

^b Discovery group acronyms (where appropriate – see text for details) or lead author of the discovery alert.

^c Classification group acronyms (where appropriate – see text for details) or lead author of the classification alert.

^d Phase with respect to maximum light (where appropriate) for the best *spectroscopic match*, as reported by the classifying group. SNe II do not typically have a clearly identifiable spectroscopic phase so are listed as “(unk)” (i.e., unknown). Very young SNe II (with very blue featureless continua) similarly have ambiguous phases so are listed as “(young)”.

In Table 4 the discovery and classification groups are listed either as acronyms of the group name, or listed as the first author in the discovery/classification notice. The acronyms used in the table for discovery groups are:

- ASAS-SN: the All-Sky Automated Survey for Supernovae (Shappee et al. 2014)
- CHASE: the CHilean Automatic Supernova sEarch (Pignata et al. 2009)
- CRTS: the Catalina Real-Time Transient Survey (Drake et al. 2009)
- Gaia: transient alerts from Gaia (e.g., Wyrzykowski et al. 2012; Blagorodnova et al. 2014, 2016)
- ISSP: the Italian Supernova Search Program
- LOSS: the Lick Observatory Supernova Search (Ganeshalingam et al. 2010)
- LSQ: the La Silla-QUEST low redshift supernova survey (Baltay et al. 2013)
- MASTER: the Mobile Astronomical System of Telescope-Robots (Lipunov et al. 2004)
- OGLE: the OGLE-IV real-time transient search (Wyrzykowski et al. 2014)
- PanSTARRS: the Panoramic Survey Telescope and Rapid Response System panstarrs
- PTF/iPTF: the Palomar Transient Factory (Rau et al. 2009; Law et al. 2009) and its successor
- SkyMapper: the SkyMapper (Keller et al. 2007) transients search
- TAROT: the Télescope á Action Rapide pour les Objets Transitoires (Rapid Action Telescope for Transient Objects) at La Silla (e.g., Klotz et al. 2013)
- TNTS: the Tsinghua-NAOC Transient Survey

The acronyms used in the table for classification groups are:

- ASP: the Asiago Supernova Program (Tomasella et al. 2014)
- AWSNAP: the ANU+WiFeS SuperNovA Program (this work)
- CSP: the Carnegie Supernova Project (Folatelli et al. 2013)
- LCOGT: the Las Cumbres Observatory Global Telescope (Brown et al. 2013)
- PESSTO: the Public ESO Spectroscopic Survey for Transient Objects (Smartt et al. 2015)
- SNF: SuperNova Factory (Aldering et al. 2002)

Some transients in Table 4 are known by other aliases or are listed in shorthand form (due to a lengthy full name). These transients and their aliases (or full names) are noted in Table 5.

Table 5 Alternate and/or full designations for SNe in the AWSNAP sample

SN	Alias
SN 2013ef	ASASSN-13bb
SN 2014E	PTF14w
SN 2014cx	ASASSN-14gm
SN 2014dq	ASASSN-14jb
SN 2015L	ASASSN-15lh
iPTF13dge	PS1-13dvn
LSQ15adm	Gaia15aep
LSQ15ey	PS15ii
PS15ae	CSS141223:113342+004332
PSNJ09023787+2556042	Gaia15aet
PSNJ10433393-3048206	PS15ip
PSNJ20250386-2449133	PS15bjv
SNhunt222	LSQ14rl
CSS1222	PS1-14ya
CSS1222	CSS140326:122257+282955
MASTERJ1408	MASTER OT J140804.26-115949.7
MASTERJ1353	MASTER OT J135329.90-421622.5
MASTERJ0746	MASTER OT J074610.09-712224.9

Table 6. All AWSNAP Sp

SN	Observation Date	Grating	Exposure Time (s)
SN 2009ip	2012-Oct-22	B3000	1200
SN 2009ip	2012-Oct-22	R3000	1200
SN 2009ip	2012-Oct-23	B7000	1200
SN 2009ip	2012-Oct-23	R7000	1200
SN 2009ip	2012-Sep-22	B3000	1200
SN 2009ip	2012-Sep-22	R3000	1200
SN 2009ip	2012-Sep-23	B3000	1200
SN 2009ip	2012-Sep-23	R3000	1200
SN 2009ip	2013-Apr-12	B7000	1200
SN 2009ip	2013-Apr-12	R7000	1200

Note. — Abbreviated version – full version of this table included in arXiv package.

AWSNAP spectra: The full list of AWSNAP spectra released here is given in Table 6, along with pertinent observation details such as grating and exposure time.

SN Ia sodium fits: In Table 7 we present the best fit parameters (and uncertainties) for our fits to narrow sodium absorption in our sample of SN Ia maximum light spectra. Table 8 lists the redshifts used to establish the local rest velocity of the SN – typically this was the redshift of the host galaxy but occasionally is obtained from galaxy emission features at the location of the SN (denoted as “Local”).

Table 7 Fits of Na line in SNe Ia

SN	Observation Date	Grating	v_{Na} (km s ⁻¹)	σ_{Na} (km s ⁻¹)	pEW_{Na} (Å)
ASASSN-14hr	2014-Oct-03	R3000	-41.3 ± 16.5	76.3 ± 13.6	0.74 ± 0.17
ASASSN-14jc	2014-Oct-27	R3000	-2.8 ± 11.5	65.3 ± 10.6	0.98 ± 0.19
ASASSN-14jg	2014-Nov-06	R3000	8.9 ± 15.3	58.1 ± 15.2	0.23 ± 0.07
ASASSN-15go	2015-Apr-11	R3000	82.9 ± 12.1	70.0 ± 10.6	1.75 ± 0.32
iPTF13dge	2013-Sep-19	R7000	-35.1 ± 3.3	22.3 ± 3.4	0.34 ± 0.05
LSQ14bcj	2014-Apr-23	R7000	20.9 ± 4.7	28.0 ± 4.9	0.99 ± 0.19
PS1-14wl	2014-Apr-02	R3000	35.9 ± 12.9	70.0 ± 0.0	1.22 ± 0.22
PSNJ13471211-2422171	2015-Feb-15	R3000	14.5 ± 49.6	119.4 ± 35.9	0.71 ± 0.26
PSNJ17194328-7721305	2013-Aug-30	R7000	-70.7 ± 3.2	24.3 ± 3.4	0.47 ± 0.07
SN 2012dn	2012-Jul-21	R3000	-9.4 ± 19.8	79.0 ± 17.2	0.25 ± 0.07
SN 2013aj	2013-Mar-08	R3000	5.0 ± 24.5	95.2 ± 18.8	0.43 ± 0.11
SN 2013cg	2013-May-26	R7000	42.0 ± 23.2	118.9 ± 16.6	1.39 ± 0.25
SN 2013cy	2013-Jun-03	R3000	45.2 ± 19.0	42.5 ± 20.8	0.19 ± 0.11
SN 2013er	2013-Jul-31	R3000	11.4 ± 16.3	78.4 ± 13.3	2.05 ± 0.44
SN 2013gh	2013-Aug-30	R7000	-18.9 ± 3.0	23.3 ± 3.1	1.50 ± 0.22
SN 2014aa	2014-Mar-14	R3000	-4.7 ± 43.5	130.0 ± 0.0	1.42 ± 0.34
SN 2014ao	2014-Apr-23	R7000	-7.2 ± 3.1	23.7 ± 3.2	1.33 ± 0.19
SN 2014at	2014-Apr-23	R3000	0.3 ± 41.8	130.0 ± 0.0	0.40 ± 0.14
SN 2014bx	2014-Jul-22	R3000	55.4 ± 12.9	73.7 ± 10.9	4.34 ± 0.79

Table 8 Host Galaxy Redshifts for SN Ia Na sample

SN	Host	Redshift	Ref. ^a
ASASSN-14hr	2MASX J01504127-1431032	0.033620	6dF (Jones)
ASASSN-14jc	2MASX J07353554-6246099	0.011320	6dF (Jones)
ASASSN-14jg	PGC 128348	0.015315	Local
ASASSN-15go	(unknown)	0.019030	Local
iPTF13dge	NGC 1762	0.015854	(Theureau et al. 1998b)
LSQ14bcj	MCG -02-36-015	0.036056	Local
PS1-14wl	2MASX J13324055-2036204	0.032346	Local
PSNJ13471211-2422171	ESO 509-G108	0.019910	(Ogando et al. 2008)
PSNJ17194328-7721305	ESO 044-G010	0.009587	Local
SN 2012dn	ESO 462-G016	0.010187	(Theureau et al. 1998b)
SN 2013aj	NGC 5339	0.009126	(Theureau et al. 1998b)
SN 2013cg	NGC 2891	0.007952	(Ogando et al. 2008)
SN 2013cy	ESO 532-G025	0.031465	(da Costa et al. 1991)
SN 2013er	IC 850	0.018052	(Grogin et al. 1998)
SN 2013gh	NGC 7183	0.009075	Local
SN 2014aa	NGC 3861	0.016982	(Cortese et al. 2008)
SN 2014ao	NGC 2615	0.014663	Local
SN 2014at	NGC 7119	0.032242	(Donzelli & Pastoriza 2000)
SN 2014bx	NGC 6808	0.011570	(Sandage & Tammann 1981)

^a Via NED. “Local” denotes local velocity measured with WiFeS, either from narrow lines in the SN spectrum or from galaxy rotation characteristics (see text for details).